Int J Adv Manuf Technol (2011) 55:945–954
DOI 10.1007/s00170-010-3142-0

ORIGINAL ARTICLE

# Numerical simulation of thermal behavior during laser direct metal deposition

**Gangxian Zhu · Anfeng Zhang · Dichen Li · Yiping Tang · Zhiqiang Tong · Qiaopan Lu**

Received: 23 July 2010 / Accepted: 29 December 2010 / Published online: 20 January 2011


**Abstract** To discuss the influence of thin-walled blade's curvature change and accumulating layer number on the temperature field distribution in laser direct metal deposition and obtain a uniform thickness of a thin-walled blade, the temperature field distribution was calculated by numerical simulation. The thin-walled blade's curvature change and accumulating layer number can be studied, respectively. The effect of accumulating layer number on temperature field distribution was studied by thin wall; the effect of curvature change on temperature distribution was investigated by thin-walled rings with different curvatures. The numerical results show that the molten pool temperature of the thin wall increases with the layer number, and the molten pool temperature of thin-walled ring increases with the its curvature. The rules of laser power changing with the layer number and curvature in the processing of the thin-walled blade can be obtained by simulation when keeping molten pool temperature stable. According to the numerical results, the thin-walled blades were fabricated by experiments. The experimental results show that the laser power should be changed with the layer number and curvature if a uniform thickness of the blade can be obtained, which is in agreement with the numerical simulation.

**Keywords** Laser direct metal deposition · Thin-walled part · Curvature change · Numerical simulation

G. Zhu · A. Zhang · D. Li (✉) · Y. Tang · Z. Tong · Q. Lu
State Key Laboratory for Manufacturing Systems Engineering,
Xi'an Jiaotong University,
Xi'an 710049, People's Republic of China
e-mail: dcli@mail.xjtu.edu.cn

G. Zhu
e-mail: gxzhu2005@stu.xjtu.edu.cn

## 1 Introduction

Laser direct metal deposition (LDMD) is a very promising process for the rapid fabrication of fully dense steel components directly from a CAD model [1–4]. LDMD is a process which builds solid metallic parts by injecting metal powder into a laser-generated molten zone. After deposition of each layer, the powder delivery nozzle and the laser beam head are raised in the *z*-direction. Accordingly, the part is then built line by line and layer by layer.

Control of the molten pool size, which is dependent on the molten pool temperature, is a critical issue since it impacts the quality of the product. Therefore, a thorough understanding of the molten pool temperature distribution is imperative. Much research work has been carried out in this field. Pinkerton and Li developed a simple thermal model to analyze the temperature distribution and estimate the molten pool size [5]. Liu and Li established a model to investigate the effects of process parameters on the layer thickness, powder utilization rate, and forming speed of thin-walled parts [6]. Labudovic et al. studied the effects of laser-processing parameters (laser power and scanning speed) on the molten pool size [7]. Wang et al. developed a three-dimensional finite element model to optimize molten pool size for each layer [8, 9]. And other scholars built numerical models to simulate the temperature history during LDMD process [10–14].

In the existing research, the effects of process parameters, material properties, environmental conditions, and deposition process on the molten pool temperature were discussed. However, there are few systematic studies on the effect of the parts' curvature change on the molten pool temperature, as shown in Fig. 1. In the present work, a three-dimensional finite element model was built to simulate multilayer LDMD of 316L stainless steel

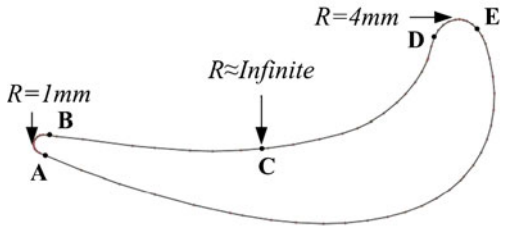


**Fig. 1** Schematic diagram of thin-walled blade with different curvatures

(316LSS) powder using the ANSYS software package. The model considers a Gaussian distribution of heat flux from a moving heat source with a conical shape. The laser power was optimized in order to achieve a predefined molten pool temperature. The thermal cycles were calculated for a 15-layer LDMD process. According to layer number and curvature, the rules of laser power changing in the processing of the thin-walled blade were obtained by simulation under keeping the molten pool temperature stable condition. Finally, based upon the predicted laser power of each layer, the thin-walled blades were fabricated by experiments.

## 2 Finite element modeling

The effects of the thin-walled blade's curvature change and accumulating layer number on the molten pool temperature field distribution can be studied, respectively. The effect of accumulating layer number on temperature field distribution was studied by thin wall; the effect of curvature change on temperature distribution was investigated by thin-walled rings with different curvatures. The influence of thin-walled blade's curvature change and accumulating layer number on the temperature field distribution can be obtained by combining the effects of layer number and curvature change. The thin-walled rings with different curvatures can be replaced by different radiuses.

### 2.1 Geometric model of thin-walled rings

To predict the temperature distribution of thin-walled rings in LDMD process, a three-dimensional finite element model was built to simulate the LDMD process using ANSYS. The geometry and finite element mesh used in the model are shown in Fig. 2.

### 2.2 Heat transfer equation and analysis

To calculate the temperature distribution, the finite element method was used to numerically solve the following heat transfer equation:

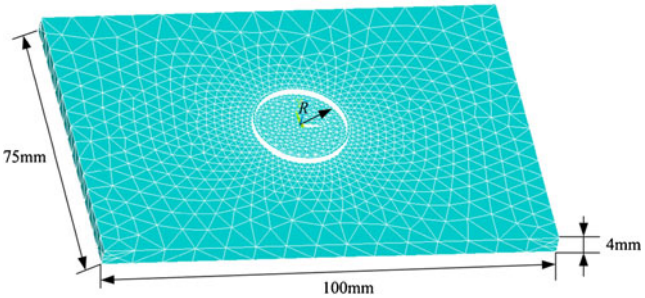


**Fig. 2** Finite element mesh and geometry

$$\rho c\frac{\partial T}{\partial t}=Q+\frac{\partial}{\partial x}\left(K_{\mathrm{x}}\frac{\partial T}{\partial x}\right)+\frac{\partial}{\partial y}\left(K_{\mathrm{y}}\frac{\partial T}{\partial y}\right)+\frac{\partial}{\partial z}\left(K_{\mathrm{z}}\frac{\partial T}{\partial z}\right) \tag{1}$$

Where $T$ is temperature, $t$ is time, $\rho$ is density, $c$ is specific heat, and $K_x$, $K_y$, and $K_z$ is the thermal conductivity at $x$-, $y$-, and $z$-direction, respectively.

The most significant heat transfer mechanisms in LDMD refer to the heat input from the heat source and the heat losses due to conduction, convection, and radiation from the deposition layer surfaces. In the present investigation, radiation was ignored.

### 2.3 Heat input

In order to simulate the heat input distribution, the laser beam is modeled as a Gaussian profile of heat flux produced by a moving heat source with a conical shape. During LDMD process, part of the energy generated by the laser beam is lost before being absorbed by the deposited material. Measurements in Ref. [15] revealed that the laser energy transfer efficiency was in the range of 30–50%. This indicates that more than half of the incident laser energy is not transferred to the deposited material. Several factors can reduce the net absorbed laser energy: partial reflection on the deposited metal, absorption by in-flight powder and absorption by evaporating metal from the pool [8]. The Gaussian distribution of heat flux can be computed according to the formula [16]:

$$-k\frac{\partial T}{\partial z}=\eta\frac{Q}{\pi R^2}\exp\left(\frac{-2r^2}{R^2}\right).....r\le R \tag{2}$$

Where $Q$ is laser power (W), $\eta$ is utilization rate of laser, $R$ is laser beam radius, and $r$ is the distance from the point which is located inside the beam to the center of beam.

**Table 1** Material properties of 316L stainless steel [17]

| Temperature(°C) | Specific heat (J/kg°C) | Conductivity (W/m°C) | Density (1.0E3 kg/m$^3$) |
|---|---|---|---|
| 20 | 477 | 12.6 | 8 |
| 100 | 496 | 14.7 | 8 |
| 200 | 515 | 16.3 | 8 |
| 300 | 525 | 18.0 | 8 |
| 400 | 550 | 19.8 | 8 |
| 500 | 577 | 20.8 | 8 |
| 600 | 582 | 22.6 | 8 |
| 700 | 611 | 23.9 | 8 |
| 800 | 640 | 25.5 | 8 |
| 900 | 669 | 26.4 | 8 |
| 1,000 | 675 | 27.5 | 8 |
| 1,100 | 711 | 28.6 | 8 |
| 1,200 | 739 | 29.7 | 8 |
| 1,430 | 760 | 31.7 | 8 |
| 2,000 | 812 | 42 | 8 |

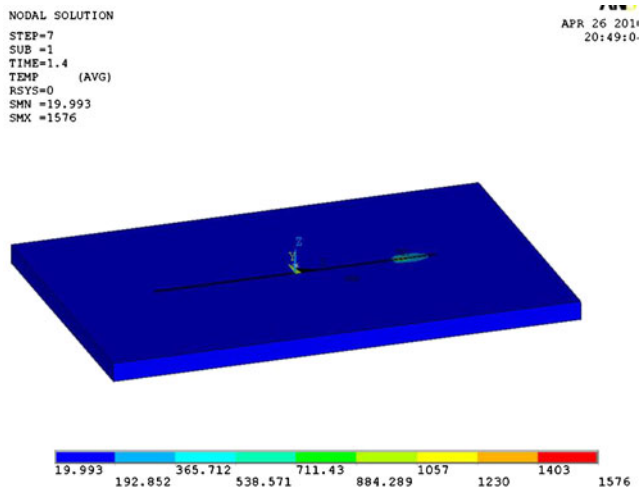


(a)

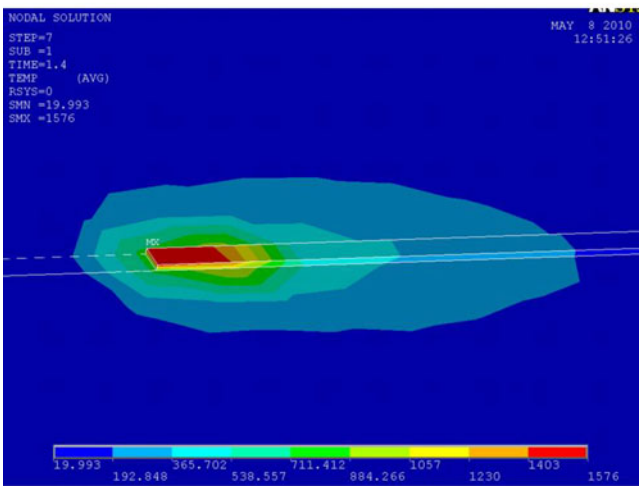


(b)

**Fig. 3** The temperature field distribution with the 1st-layer number; **a** global and **b** local

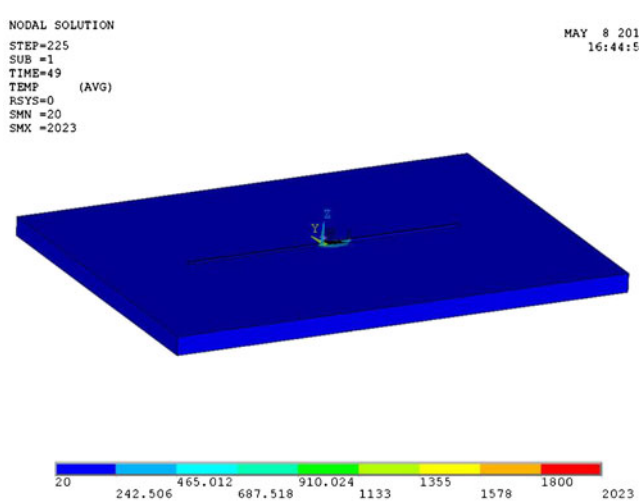


(a)

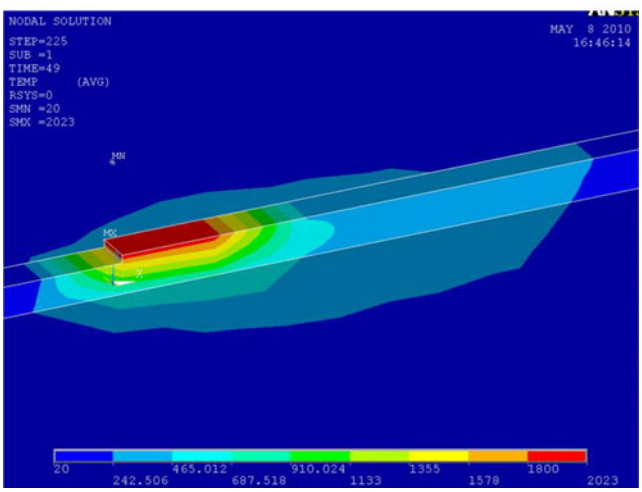


(b)

**Fig. 4** The temperature field distribution with the 5th-layer number; **a** global and **b** local

### 2.4 Material properties

Because the material thermophysical behaviors have a great impact on the accuracy of numerical simulation results, the finite element heat transfer analysis requires accurate values of thermal conductivity, specific heat, material density, and latent heat of fusion. The thermal physical behaviors are dependent on temperature, as shown in Table 1 [17].

### 2.5 Initial and boundary conditions

To resolve heat transfer equations, the initial and boundary conditions are needed in the computational domain. The three boundary conditions can be concluded as follows:

$$T = T^* \tag{3}$$

$$K_x \frac{\partial T}{\partial x} n_x + K_y \frac{\partial T}{\partial y} n_y + K_z \frac{\partial T}{\partial z} n_z = q \tag{4}$$

$$K_x \frac{\partial T}{\partial x} n_x + K_y \frac{\partial T}{\partial y} n_y + K_z \frac{\partial T}{\partial z} n_z = h(T_a - T) \tag{5}$$

Where $K$ is the thermal conductivity, $h$ is the convective heat transfer coefficient, $T_a$ is the ambient temperature around the part, which is considered to be equal to room temperature.

Besides all the heat conduction equations boundary conditions, the initial temperature must be set, which is considered as initial condition.

$$T(x,y,z,t)|_{t=0} = T_0 \tag{6}$$

The latent heat of fusion is simulated by a manual input in the specific heat according to Brickstad and Josefson

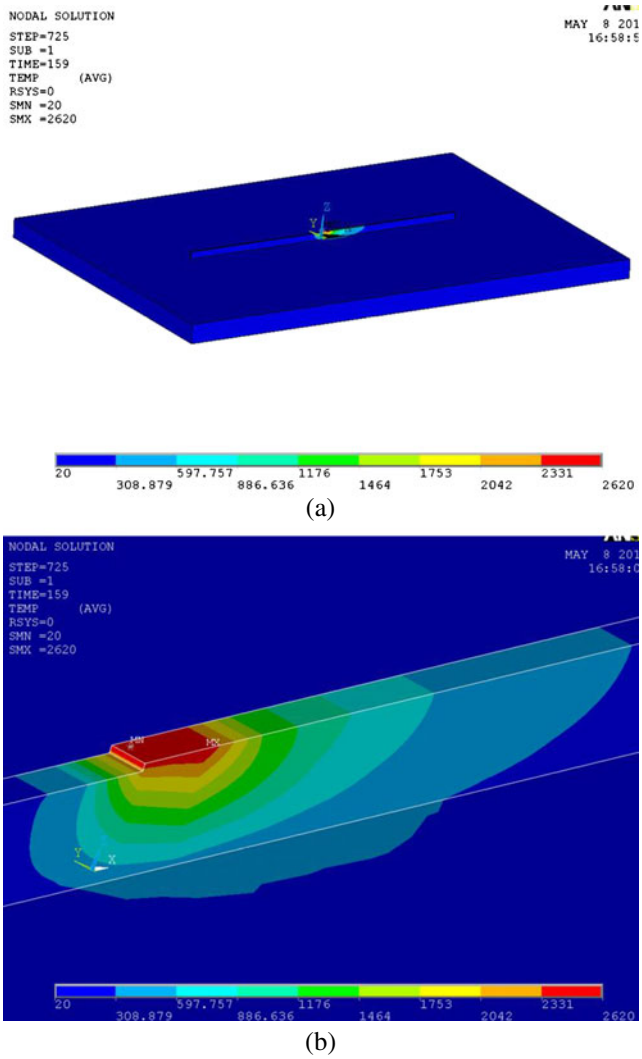


**Fig. 5** The temperature field distribution with the 15th layer number; **a** global and **b** local

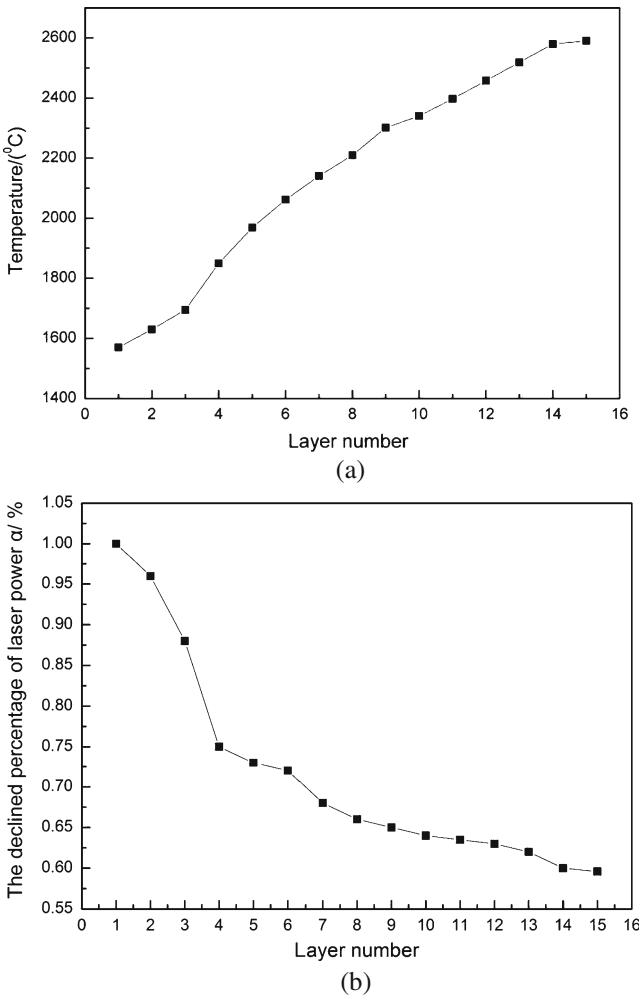


**Fig. 6** The relationship between the temperature distribution and the trend of laser power and layer number; **a** the temperature distribution and **b** the trend of laser power changing

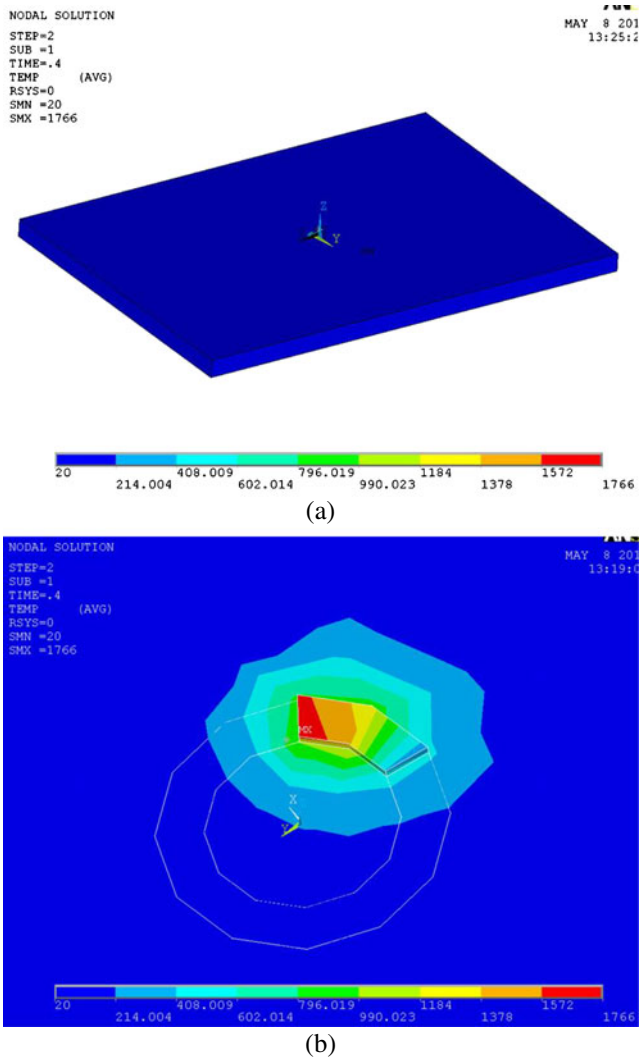


**Fig. 7** The temperature field distribution with the radius of 1 mm; **a** global and **b** local

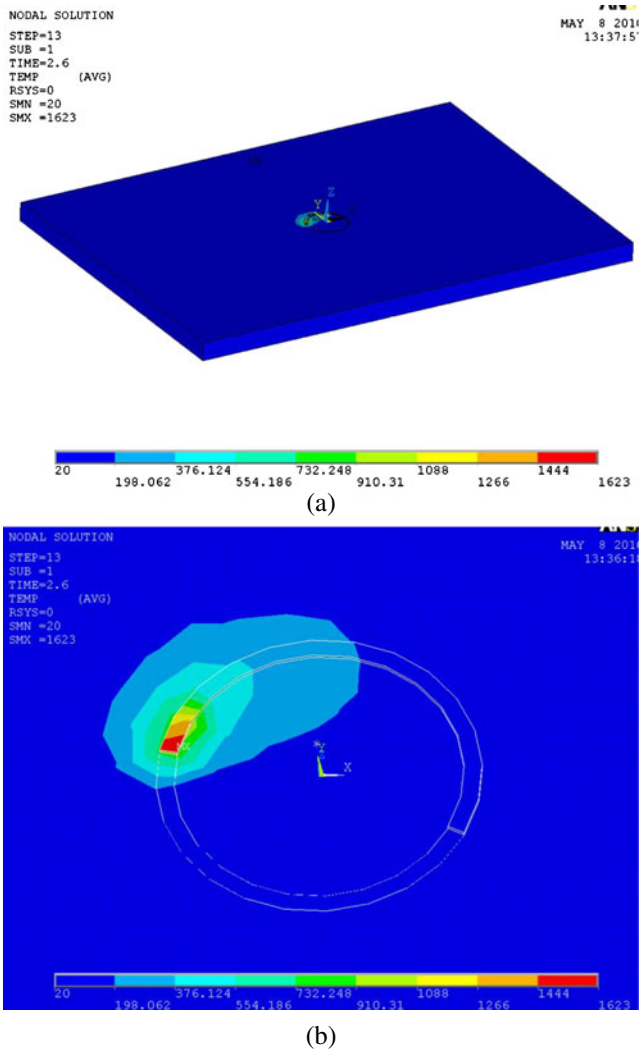


**Fig. 8** The temperature field distribution with the radius of 4 mm; **a** global and **b** local

[18]. The relationship among enthalpy ($H$), density ($\rho$), and specific heat ($c$) is:

$$\Delta H(T) = \int_0^T \rho c(t)\mathrm{d}t \tag{7}$$

Where $H$ is the enthalpy.

## 3 Results and discussions

Through preliminary experiments, the basic process parameters were optimized with the use of 6 mm/s scanning speed and 250 W laser power. The laser energy transfer efficiency is set to 0.35 [19]. The substrate material utilized was also 316LSS.

The molten pool temperature distributions were calculated with different layer numbers of thin wall and different

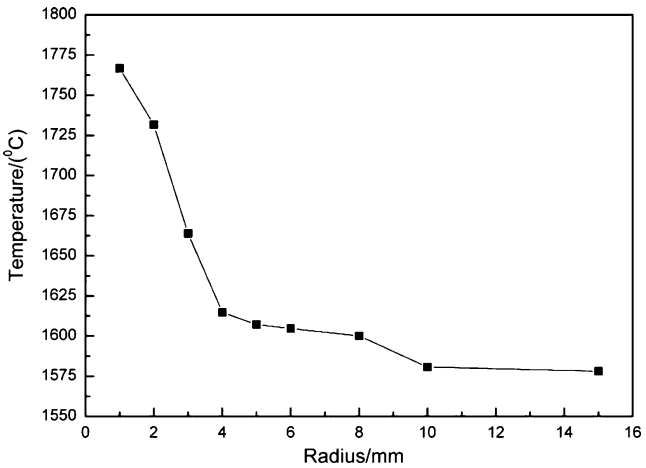


**Fig. 9** The relationship between temperature distribution and radius

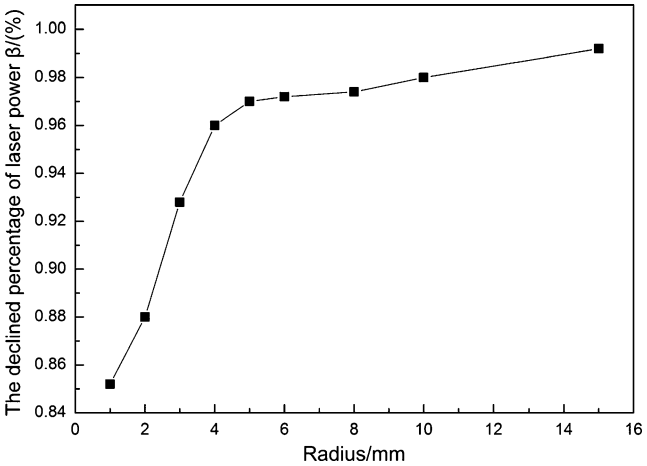


**Fig. 10** The trend of laser power changing with different radiuses

radiuses of thin-walled rings, respectively. Because of the fluctuation of molten pool temperature in each layer, the mean temperature of each layer is considered as the temperature of the deposition layer.

### 3.1 The influence of accumulating layer number on the molten pool temperature

The model dimension along *x*-, *y*-, and *z*-axes direction of thin wall is $60\times0.5\times3$ mm$^3$. The calculation is performed for the deposition from the first layer to the last layer (the 15th layer). Figures 3, 4, and 5 show the typical temperature field distributions of the fabricated thin wall with different layer numbers. The calibrated model was then used to simulate the entire 15-layer LDMD process. The temperature distributions with layer number were shown in Fig. 6a under constant laser power condition. Based on the 1,570°C produced by temperature field computation of the first deposited layer, the trend of laser power changing could be obtained with layer by layer by keeping a constant molten pool temperature, as shown in Fig. 6b.

It is observed from Fig. 6a that the calculated temperature increases with the layer number. Because the substrate is cold during deposition of the first few layers, and as more layers are deposited, they act as a barrier to heat conduction to the substrate, the part becomes hotter and the temperature increases with the layer number. In order to achieve a steady temperature distribution surrounding the molten pool, the laser power must be adjusted for each layer. Figure 6b shows the laser power applied for each layer when keeping the molten pool temperature stable. Provided that the laser power of the first deposition layer is denoted by *P*. The declined percentages of laser power are denoted by $\alpha$ with the increasing layer number when the temperature of each layer is consistent with the temperature of the first layer. Then the laser power of any layer can be calculated by $P\times\alpha$ under keeping the molten pool temperature of each layer stable. It is observed that the laser power decreases with the layer number.

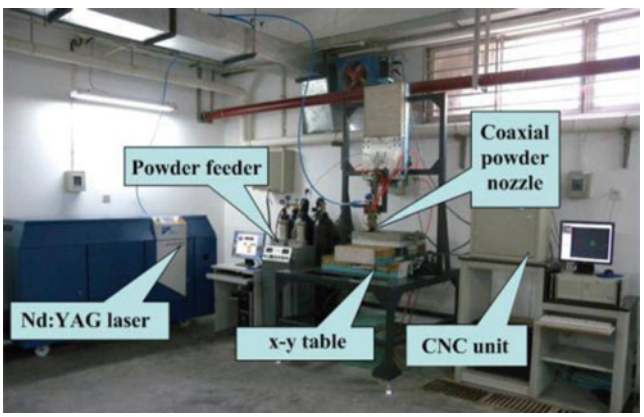


**Fig. 11** Schematic diagram of experimental setup

**Table 2** Composition of the 316LSS powder

| Element | Wt.% |
|---|---|
| C | 0.024 |
| Si | 0.51 |
| Mn | 1.53 |
| P | 0.024 |
| S | 0.003 |
| Cr | 16.75 |
| Ni | 10.17 |
| Mo | 2.05 |
| Fe | Base |

### 3.2 The influence of curvature change of thin-walled rings on the molten pool temperature

The thin-walled rings with different curvatures can be handled by defining different radiuses. To investigate the

**Table 3** Basic process parameters for the fabrication of thin-walled blade samples

| Parameter | Value |
|---|---|
| Table feeding rate (m/s) | 0.006 |
| Beam diameter (m) | 0.00048 |
| Powder mass flow rate (kg/s) | 0.00013 |
| Shielding gas (Ar), flow rate (m$^3$/h) | 0.43 |
| Carrier gas (Ar), flow rate (m$^3$/h) | 0.48 |
| *z*-Increment (m) | 0.0002 |

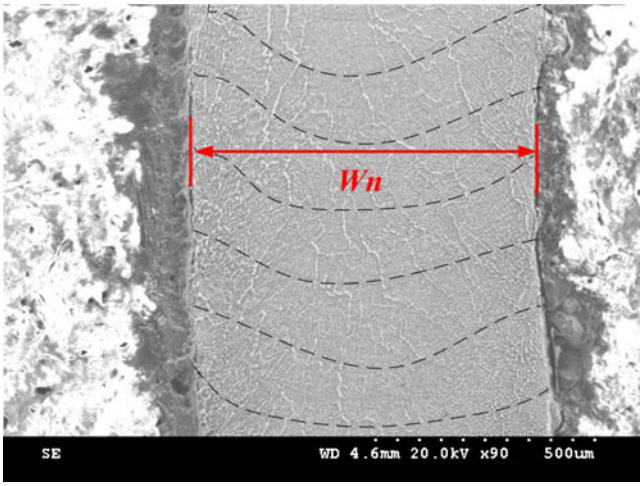


**Fig. 12** The cross section of thin-walled blade samples

influence of different thin-walled rings' radiuses on the molten pool temperature, the molten pool temperature distribution is studied with the radius of $R$=1, 2, 3, 4, 5, 6, 8, 10, and 15 mm when depositing the first layer. Figures 7 and 8 show the typical temperature field distributions of the thin-walled rings with the radius of 1 and 4 mm, respectively. The relationship between temperature distribution and radius was shown in Fig. 9.

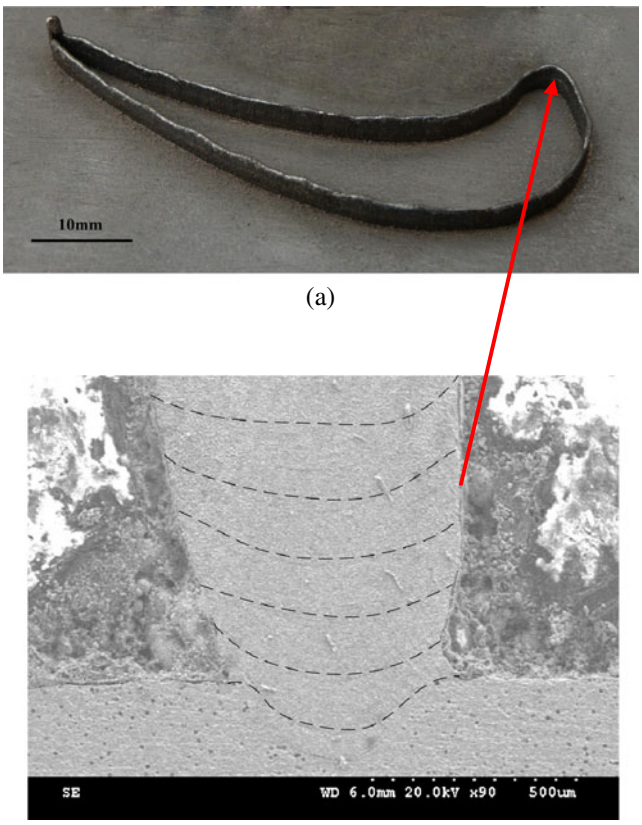


**Fig. 13** Photos of the thin-walled blade sample with constant laser power; **a** the thin-walled blade sample and **b** the cross section

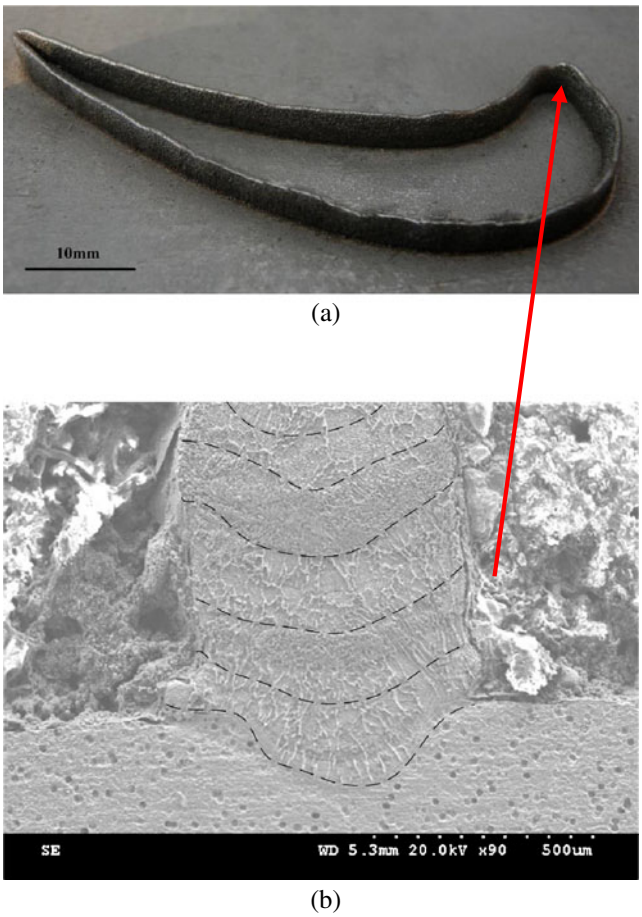


**Fig. 14** Photos of the thin-walled blade sample with varied laser power; **a** the thin-walled blade sample and **b** the cross section

As can be seen from Fig. 9, the molten pool temperature decreases with the radius, namely, the molten pool temperature increases with the curvature. It is also observed that the molten pool temperature tends to be gentle when the radius is more than 4 mm. This indicates that the influence of the radius on the molten pool temperature is weak when the radius is more than 4 mm.

In order to keep the molten pool temperature stable for different radiuses, the trend of laser power changing can be obtained based on the 1,570°C produced by temperature field computation of the thin wall's first layer. And the relationship between laser power and radius was shown in Fig. 10.

According to section 3.1, the laser power of any layer can be calculated by $P\times\alpha$ under keeping the molten pool temperature of each layer stable. To keep the temperature distributions of the thin-walled rings with different curvatures consistent with the thin wall, the decline percentages

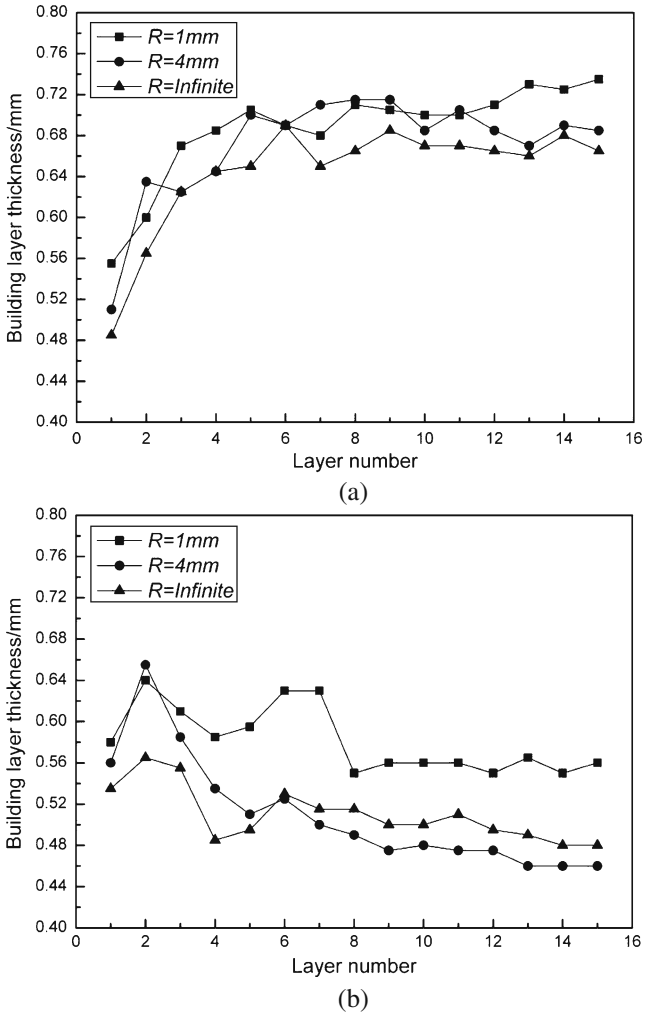


**Fig. 15** The relationship between building thickness and layer number; **a** with constant laser power and **b** with varied laser power

of laser power are denoted by $\beta$ with the increasing curvature.

Combining Fig. 6b and 10, the trend of laser power changing with layer number and curvature can be obtained under keeping melt pool temperature stable. The laser power of the first deposition layer used is denoted by *P*. The declined percentages of laser power are denoted by $\alpha$ with the layer number and $\beta$ with the curvature. Then the laser power of any layer and any curvature can be calculated by $P \times \alpha \times \beta$.

## 4 Experimental investigations

To verify the correctness and rationality of numerical computation, a thin-walled blade sample was fabricated by experiments. The experiments were carried out with the equipment shown in Fig. 11. The system includes a Nd/YAG laser with a 1 kw maximum output power, a three-axis computer numerical control (CNC) worktable and a powder supply system. The laser beam was guided to the worktable through an optical fiber and focused by a lens with a 160-mm focal length. The powder used was 316LSS with spherical shape and its diameter is 15~45 μm. The substrate material utilized in experiments was 316LSS with a dimension of $100 \times 75 \times 4$ mm$^3$. The compositions of the powder are shown in Table 2.

To agree with simulation computation, the laser power is set to 250 W in the first layer in experiments, and other process parameters are shown in Table 3. The laser power was preset in a CNC system before experiments. The thin-walled blade samples were built under two different conditions: constant laser power and varied laser power. The layer number of the two parts is 15. After experiments the cross sections of thin-walled blade samples were obtained by cutting, grinding, polishing and metallographical etching, and then the thickness of each layer can be measured under Hitachi S-3000N scanning electron microscope as shown in Fig. 12.

Two thin-walled blade samples were built with constant laser power and varied laser power, respectively. According to numerical results, the varied laser power was carried out

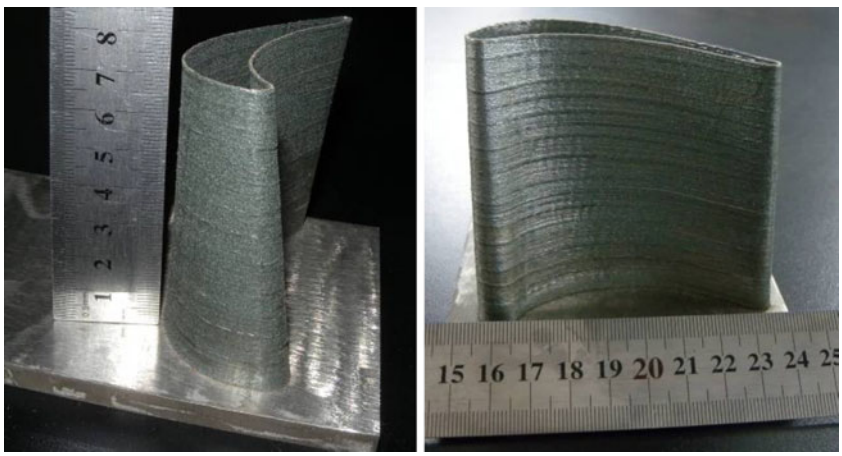

**Fig. 16** A thin-walled blade sample

as follows: the laser power is changed with layer number, and in each layer the laser power is also different at the corners of $R$=1 mm (AB region) and $R$=4 mm (DE region) in Fig. 1. The pictures of the two parts with 15 layers are shown in Figs. 13 and 14.

Figure 13 shows the sample and its cross-section fabricated with the constant laser power of 250 W. We can see that the height on the top layer of the sample is uneven, and the corner is abnormally higher than other places in the scanning path.

At the sharp corners in the path, the movement controller of CNC system has to vary its vector velocity to change the movement direction in Fig. 13. Because the worktable of the CNC-machine decelerated and then accelerated at the corner, whereas the laser was on, the traveling speed of CNC table at the corner is lower and the energy and powders at the corner may be higher than other normal places. As a result, the effects resulted in excessive build-up. Simultaneously, the thickness of the thin-walled blade is increased from the bottom to the top. This is due to the change of the molten pool temperature field distribution during the whole depositing process. As displayed in Fig. 6, it can be recognized that at the beginning the temperature increased very rapidly with the layer number because the workpiece was cold and the heat conductivity (three dimensional) was high and the thickness is nonuniform in the first a few layers. After about 14 layers, with decreasing heat conduction (two dimensional), the heat exchange reached a quasi-steady status. Thus, the molten pool temperature increased slowly.

To improve the forming quality of the sample and control, the molten pool temperature, the varied laser power was pre-set in CNC system according to the numerical results. Figure 14 shows the sample and its cross section. The sample exhibits no excessive build-up but a homogeneous thickness.

The thicknesses with layer number were measured at three positions: $R$=1 mm, $R$=4 mm, and $R \approx infinite$ under the two different conditions. Figure 15 shows the relationship between layer thickness and layer number under two laser power conditions, respectively.

As can be seen from Fig. 15a, the layer thickness increases gradually with the layer number and decreases with the radius. Figure 15b shows that the thickness of the sample is uniform compared to Fig. 15a under the varied laser power condition.

To obtain the uniform thickness of thin-walled blades and keep molten pool temperature constant with layer number, the laser power was reduced continuously with layer number due to less conduction through the workpiece. When heat equilibrium arrived, the laser power was no longer falling. However, the thickness at the same layer was not uniform due to curvature change. The reason is that the size of the molten pool at the corners was bigger than the other normal places due to the accumulating energy, so the laser power was reduced further at the corners.

By using above parameters, a thin-walled blade sample was fabricated as shown in Fig. 16. The actual building height of the thin-walled blade sample is 77.56 mm, and the designed height is 78 mm.

## 5 Conclusions

1. The effects of thin-walled blade's curvature change and accumulating layer number on the temperature field distribution were calculated and the trend of laser power changing with the layer number and curvature in the processing of the thin-walled blade can be obtained by simulation when keeping molten pool temperature stable.
2. The thicknesses of the thin-walled blade samples were investigated with constant and varied laser power by experiments. The experimental results show that the excessive build-up occurred with constant laser power because of the increase of energy density at corners and the thickness with varied laser power is more uniform than the constant laser power.

**Acknowledgments** The work was financially supported by the State Basic Research Key Projects of China through Grant no. 2007CB707704, the National Natural Science Foundation of China through Grant no. 50675171, and Program for Changjiang Scholars and Innovative Research Team in University (PCSIRT0646).

## References

1. Mah R (1997) Directed light fabrication. Adv Mater Process 151 (3):31–33
2. Lewis GK, Schlienger E (2000) Practical considerations and capabilities for laser assisted direct metal deposition. Mater Des 21(4):417–423
3. Wohlers TT (2006) Wohlers Report 2006. Wohlers Associates Inc, USA, pp 13–43
4. Zhong ML, Liu WJ (2008) Leading Areas and Hot Topics on Global Laser Materials Processing Research. Chin J Lasers 35 (11):1653–1659
5. Pinkerton AJ, Li L (2004) The significance of deposition point standoff variations in multiple-layer coaxial laser cladding (coaxial cladding standoff effects). Int J Mach Tools Manuf 44 (6):573–584. doi:10.1016/j.ijmachtools.2004.01.001
6. Liu JC, Li LJ (2007) Effects of process variables on laser direct formation of thin wall. Opt Laser Technol 39(2):231–236. doi:10.1016/j.optlastec.2005.08.012
7. Labudovic M, Hu D, Kovacevic R (2003) A three dimensional model for direct laser metal powder deposition and rapid prototyping. J Mater Sci 38(1):35–49. doi:10.1023/A:1021153513925

8. Wang L, Felicelli S, Gooroochurn Y, Wang PT, Horstemeyer MF (2008) Optimization of the LENS (R) process for steady molten pool size. Mater Sci Eng A 474(1–2):148–156. doi:10.1016/j.msea.2007.04.119
9. Wang L, Felicelli S (2006) Analysis of thermal phenomena in LENS™ deposition. Mater Sci Eng A 435:625–631. doi:10.1016/j.msea.2006.07.087
10. Long RS, Liu WJ, Xing F, Wang HB (2008) Numerical simulation of thermal behavior during laser metal deposition shaping. Nonferr Met Soc 18(3):691–699. doi:10.1016/S1003-6326(08)60120-X
11. Jendrzejewski R, Kreja I, Sliwinski G (2004) Temperature distribution in laser-clad multi-layers. Mater Sci Eng A 379(1–2):313–320. doi:10.1016/j.msea.2004.02.053
12. Ye RQ, Smugeresky JE, Zheng BL, Zhou YZ, Lavernia EJ (2006) Numerical modeling of the thermal behavior during the LENS (R) process. Mater Sci Eng A 428(1–2):47–53. doi:10.1016/j.msea.2006.04.079
13. He X, Mazumder J (2007) Transport phenomena during direct metal deposition. J Appl Phys 101:053113. doi:10.1063/1.2710780
14. Neela V, De A (2009) Three-dimensional heat transfer analysis of LENS™ process using finite element method. Int J Adv Manuf Technol 45:935–943. doi:10.1007/s00170-009-2024-9
15. Unocic RR, DuPont JN (2004) Process efficiency measurements in the laser engineered net shaping process. Metall Mater Trans B 35(1):143–152. doi:10.1007/s11663-004-0104-7
16. Frewin MR, Scott DA (1999) Finite element model of pulsed laser welding. Weld J 78(1):15–22
17. Jiang W, Yahiaoui K, Hall FR (2005) Finite element predictions of temperature distributions in a multipass welded piping branch junction. J Press Vess T ASME 127(1):7–12. doi:10.1115/1.1845450
18. Brickstad B, Josefson BL (1998) A parametric study of residual stresses in multi-pass butt-welded stainless steel pipes. Int J Pres Ves Pip 75(1):11–25
19. Hofmeister W, Griffith M, Ensz M, Smugeresky J (2001) Solidification in direct metal deposition by LENS processing. JOM J Min Met Mat S 53(9):30–34. doi:10.1007/s11837-001-0066-z